Travelling waves or sequentially activated discrete modules: mapping the granularity of cortical propagation

Yuval Orsher[1,2], Ariel Rom[1,3], Rotem Perel[1], Yoav Lahini[2,3], Pablo Blinder[1,3], Mark Shein-Idelson[1,3,*]

[1]School of Neurobiology, Biochemistry, and Biophysics, Tel Aviv University, Israel
[2]School of Physics & Astronomy, Faculty of Exact Sciences, Tel Aviv University, Israel
[3]Sagol School of Neuroscience, Tel Aviv University, Israel
*Corresponding Author - sheinmark@tauex.tau.ac.il

Abstract

Numerous studies have identified travelling waves in the cortex and suggested they play important roles in brain processing. These waves are most often measured using macroscopic methods that are unable to assess the local spiking activity underlying wave dynamics. Here we investigated the possibility that waves may not be travelling at the single neuron scale. We first show that sequentially activating two discrete brain areas can appear as travelling waves in EEG simulations. We next reproduce these results using an analytical model of two sequentially activated regions. Using this model, we were able to generate wave-like activity with variable directions, velocities, and spatial patterns, and to map the discriminability limits between travelling waves and modular sequential activations. Finally, we investigated the link between field potentials and single neuron excitability using large-scale measurements from turtle cortex ex-vivo. We found that while field potentials exhibit wave-like dynamics, the underlying spiking activity was better described by consecutively activated spatially adjacent groups of neurons. Taken together, this study suggests caution when interpreting phase delay measurements as continuously propagating wavefronts in two different spatial scales. A careful distinction between modular and wave excitability profiles across scales will be critical for understanding the nature of cortical computations.

Introduction

Cortical traveling waves are considered a ubiquitous feature of cortical dynamics and are suggested to play important roles in cortical processing [1–4]. These waves are observed across a wide range of spatial and temporal scales and exhibit a wide repertoire of propagation patterns. Travelling waves can propagate to specific directions (plane wave) [5–8], outwards from a center locus (radial waves) [9] or rotate around a phase singularity (spiral waves) [10–12]. Waves also range in their spatial extend from mesoscale waves spanning a single cortical area [5,7,13–18], to macroscale waves propagating through multiple brain areas and even across the two hemispheres [6,12,19–21]. Finally, cortical waves are characterized by different propagation velocities (from millimeters to meters per second) and frequency bands. For example, α-band oscillations (8-12Hz) travel from occipital to frontal areas [22]; γ-band (30-80Hz) auditory induced oscillations travel from anterior-to-posterior [23]; and slow wave oscillations (0.1-1Hz), occurring during sleep, travel from anterior to posterior cortical regions [6].

It is unclear how the abundance of travelling waves across large areas of cortex fits its modular structural and functional organization [24,25]. Tangential cortical connectivity is not uniform. It is higher within cortical areas (e.g., V1) or regions (e.g., visual cortex) then between areas (V1 and V2 or visual cortex and auditory cortex) [26–29]. This modularity is observed across multiple scales. Within single cortical areas, neurons are segmented into columns with high intra-column connectivity and sparser inter-column connectivity [30]. Such non-uniform connectivity is likely to restrict the spread of activity rather than to support smooth propagation of waves across the cortical sheet during which action potentials are sequentially activated in neurons as the wavefront passes. Indeed, it was suggested that one of the roles of modularity is to segregate circuits and computation [28,31] and prevent uncontrolled spread of excitability, as is evident in pathological conditions such as epileptic seizures [32].

Understanding in which scenarios travelling waves ignore cortical modularity requires defining the spatial granularity with which waves are examined and performing experimental measurements with the corresponding resolution. For example, determining whether a travelling wave entails a spreading excitation at the single neuron level requires single cell resolution measurements. In contrast, travelling waves are commonly measured with low spatial resolution technique [12,23,33,34]. This is especially true for extracranial recording such as EEG in which brain current sources are distant from the measurement electrodes and separated by diffracting elements such as the skull [35]. Even in more local intracranial measurements such as Electrocorticography (ECoG), volume conduction through low impedance media, such as the cerebro-spinal fluid, may result in substantial contribution of distant areas to local measurements and effective spatial lowpass filtering that blur out possible spatially segregated activations [36–38]. Imaging waves with more local reporters of excitability such as voltage sensitive dye (VSD) reduces the limitations imposed by large electrodes. While the spatial resolution of this method is higher, VSD measurements mostly reflect subthreshold potentials [39] with strong contribution from upper layers and long-range inputs [16,40,41]. Thus, VSDs integrate inputs from both local and distant spiking activities rather than represent local spiking excitability profiles. In addition, VSD signals may be contaminated by contribution from non-neuronal sources [42]. For example, the velocities of some travelling waves correspond to axonal propagation [2]. However, such axonal propagations do not necessarily activate the neurons in the target tissue and single cell excitability may

remain modular. While in specific cases the existence of travelling waves in single cells was measured in high resolution [7,43], this existence cannot be unambiguously generalized to all reported travelling waves, especially given the large diversity of reported wave patterns across different brain areas.

In addition to the lack of understanding of the nature of excitability underlying waves, previous studies raised the possibility that measured propagating patterns may be biased by the limitations of experimental technique used [4,9,44]. For example, when considering a scenario in which the intensity of a stationary source with a spatially decaying profile increases over time. In this scenario, additional regions cross the detection threshold at progressively longer times and may result in a false measurement of a propagating wave. To address this caveat, Muller et al introduced the Phase Latency Map (PLMs) allowing them to discriminate between a stationary bump and a travelling wave and to conclude that propagating waves were measured [9]. While PLMs address this specific caveat, measured travelling wave-like patterns (WLPs), that are not underlined by spatially continuous propagation, can be found in additional scenarios. For example, it was recently shown that a mixture of stationary sources can result in WLPs in EEG recordings [44]. Similarly, current source density reveals WLPs following sequential activation of different cortical lamina [45]. These studies raise important concerns about the propagation profiles in some systems. Despite these concerns, the criteria for differentiating WLPs from travelling waves remains unknown. Further, evidence for the existence of WLPs on the single neuron level is missing. Thus, we lack a classification of different identified travelling waves in terms of their underlying microscale excitability patterns.

Here, we use large-scale spiking measurements and simulations to examine the possibility that sequential activation of adjacent modules can be falsely identified as a travelling wave. Specifically, we first illustrate, using EEG simulations, that sequentially activating two adjacent cortical areas results in phase latency profiles resembling travelling waves. To link single neurons activation profiles with field potentials, we utilize the ex-vivo eye-brain preparation of turtle cortex in which travelling waves have been previously reported in response to visual stimulation [11,46,47]. Using dense multi electrode array (MEA) recordings, we compare local spiking activity with local field potentials (LFP) over several mm^2 of cortex. We show that while low frequency oscillations in LFP appear to propagate as a smooth travelling wave, the underlying spiking activity is better described by a sequential activation of separate cortical populations. Finally, using an analytical model, we map the conditions for identifying sequential stationary activations as traveling waves and describe the high diversity of resulting WLPs.

Methods

Eye-brain preparation and recording. Ex-vivo experiments were performed as in Shein-Idelson et al [47] at the Max Planck Institute for Brain Research in Frankfurt and Tel-Aviv University. Briefly, the turtle brain was explanted as a whole, while still attached to the eye through the optic nerve. After anterior and posterior transverse incisions, the 3-layered medial and dorsal cortices, which overlay the ventricular cavity directly, were flattened and placed on top of a multi electrode array (MEA) ventricular side down (with L3 facing the MEA). 120- or 252-channel systems (MEA2100, MEA256 by Multichannel Systems, MCS) were used for recording with titanium-nitrate electrode grids with 100µm spacing and 30µm electrode diameter (120MEA100/30iR-ITO, 256MEA100/30iR-ITO, MCS). During experiments, the tissue was constantly superfused at 10 ml/min with oxygenated turtle ACSF solution (96.5 mM NaCl, 2.6 mM KCl, 4 mM CaCl2, 2 mM MgCl2, 31.5 mM NaHCO3, 20 mM glucose, pH 7.4) at 18 °C which was bubbled with carbogen gas (95% O2, 5% CO2). Glutamine (0.5 mM) and HEPES (10 mM, H3375 Sigma) were added for increased retinal viability. Experiments were approved by Tel Aviv University ethical committee (Approval number: 04-18-016).

Visual stimulation. The eye cup was pinned to a Polydimethylsiloxane (PDMS) layer inside a MEA well. The visual stimulation was displayed on the screen, its size was reduced using an inverted Galilean telescope and it was focused onto the retina using a convex lens. The stimulation position and focus on the retina were adjusted using a set of 4 LEDs positioned at the edges of the screen and visible on the retina. These LEDs were turned off during the experiment. Stimulations were presented using a custom Matlab code and the psychophysics toolbox [48]. Stimulations consisted of sequentially presented full field flashes, squares flashing on the screen, natural images, or natural movies. In all stimulation, onset elicited a cortical response. Exact visual stimulation times were determined by changing the intensity of a small rectangle at the corner of the screen for every frame change and measuring this change using a photodiode.

Spectral Analysis. Spectral analysis was performed using Welch's method (*pWelch*, Matlab). For each trial, the power spectra were extracted for a time window starting 250ms post-stimulus and lasting 2 seconds. The 2 second window was divided into three 1 second blocks with 500ms overlap.

Hilbert transform and phase crossing. The analytic signal was calculated using Matlab's *hilbert* method after filtering (8th order Butterworth after zero padding). The signal's envelope was extracted from the norm of the analytic signal. The instantaneous phase was used to determine the oscillation's phase crossing events from the time the Analytic's angle crosses a specific phase. To remove noise from phase crossing statistics, we assessed the noise level of the phase crossings. We calculated the distribution of pre-stimulus (500 – 1000 ms) phase crossings' amplitude of 100 random trials. Phase crossings with amplitudes lower than mean+4 STDs of this distribution were ignored.

Wave Detection. Phase crossings during single oscillation cycles were grouped into waves using an algorithm which identified the progression of a given phase crossing across multiple channels. We start by selecting a seed, which is a specific phase crossing event in one channel. We next go through all nearest neighboring channels. If phase crossings within a 100ms (for 0-2Hz band or 2ms for 12-35Hz Band) temporal window are detected, the channel is added to the wave. This process is repeated for the added channels until no more spatiotemporally connected phase crossings are found. Only phase crossing events with Hilbert amplitudes above noise level were considered. ALSA analysis was focused on large waves recruiting many channels (2/3 for 0-2Hz band and 5/6 for 12-35Hz band). For first spike analysis, due to data sparseness, waves recruiting >30 channels were used.

Phase latency maps and correlations. Maps were calculated similarly to Muller et al [2]. The phase latency for each channel was defined as the time to reach a specific instantaneous phase for the ex-vivo experiment, or to the first maximum for the EEG simulations. When maps were calculated on single detected waves, and a given channel had more than one phase crossing in a single cluster, only the first phase crossing was used for the latency analysis. The phase latency distance correlations (PLDCs) for the ex-vivo preparation were calculated by first calculating the Euclidian distance of all electrodes from the wave starting point (the position of the first electrode having a phase crossing in the given wave) and calculating their Pearson correlation coefficient with the phase latencies. The PLDC for the EEG simulations were taken to be the correlation of the phase latencies with the electrodes' positions on the caudal-rostral axis.

Wave center path (WCP). WCP was calculated from the time-weighted 'Center of Mass' position on the electrode array for every time sample starting and ending in the first and last phase crossing, respectively. In each time sample (t), center of mass was calculated as follows:

$$\vec{X}_{CM}(t) = \frac{\sum_i \vec{X}_i \cdot A_i \cdot e^{\frac{-(t-t_i)^2}{2\cdot\sigma(t)^2}}}{\sum_i A_i \cdot e^{\frac{-(t-t_i)^2}{2\cdot\sigma(t)^2}}}$$

where the summation is over all phase crossings of a wave, $\vec{X}_i$ is the position of the i'th phase crossing and A_i is its Hilbert amplitude. The temporal weight was taken to be a Gaussian of the time difference between the time of the i'th phase crossing t_i, and the time sample for which the $X_{cm}(t)$ is calculated. To compensate for edge effects, the width of the Gaussian, σ, was varied according to progression along the wave:

$$\sigma(t) = \begin{cases} 2\overline{\Delta T} + \frac{8\overline{\Delta T}}{n_s/2} t & 0 \le t < n_s/2 \\ 10\overline{\Delta T} - \frac{8\overline{\Delta T}}{n_s/2}(t - n_s/2) & n_s/2 \le t < n_s \end{cases}$$

where n_s is the number of samples and $\overline{\Delta T}$ is the mean temporal difference between consecutive phase crossings, calculated by averaging over all time differences between consecutive crossing times of the wave. With this scaling in σ, the samples at the beginning and end are less biased towards future or past crossings, respectively.

Spike Sorting. Spikes were sorted using a custom-designed algorithm [47]. After sorting, all spikes were associated with a specific channel (determined by the channel in which the averaged spike amplitude was maximal). The spiking firing pattern of each channel was comprised by merging all spikes associated with the channel.

ALSA Calculation. To calculate the average local spiking activity (ALSA), each channel's firing pattern was convolved with a constant window of 100ms, and then smoothed using a gaussian window of the same temporal width. The ALSA was then taken to be the spatially weighted average of these smoothed firing rates. Only the nearest neighbors were considered (up to 4 neighbors), with the weight of each neighbor being half the weight of the center channel. Therefore, the ALSA value of channel i at time t is given by:

$$ALSA(i,t) = \frac{SmoothedFireRate(i,t) + \sum_{j \in n.n.} SmoothedFireRate(j,t)/2}{1 + \sum_{j \in n.n.} 1/2}$$

The ALSA onset times were taken to be the time of the first maximum in each channel's ALSA.
To reduce noise even further, only ALSA onsets that occurred around the time of the detected LFP wave were considered – from half of the wave duration before the start of the wave, to half of the wave duration after it ended.

DIP Test. The DIP-Test [49] is a statistic used to quantify the deviation of a distribution from unimodality. We used the MATLAB implementation by F. Mechler (DIP-test and DIP-test significance). The P-value was calculated by comparing the DIP statistic to a bootstrap sample (n=500) of the DIP statistic calculated for a uniform probability distribution function of sample size of the empirical distribution (the uniform distribution has been shown to be the "worst case" unimodal distribution). Since our data is one dimensional (first spike times, ALSA onsets or LFP phase crossings), we use the DIP-test directly on these one-dimensional distributions. In DIP analysis of first spikes, we only considered large enough waves (having at least 5/6 channels participating in the LFP wave). In addition, we only examined the first spikes (marking activity onset) and therefore only analyzed channels with spikes occurring during the waves (i.e., during the interval [T-W, T+W] where T is each wave's middle time and W is its width). When running the analysis on ALSA, were analyzed all trials with at least 4/6 channels.

Analytic calculations. Sequential activation of modules was represented by the sum of two one-dimensional Gaussians centered at x_1 and x_2 and multiplied by a temporal Gaussian centered around t_1 and t_2, respectively:

$$V(x,t) = \sum_{i=1,2} \exp\left(-\frac{(x-x_i)^2}{2\sigma_x^2} - \frac{(t-t_i)^2}{2\sigma_t^2}\right)$$

with spatial and temporal widths σ_x, σ_t. By moving to center coordinates: $\bar{x} = \frac{x_1+x_2}{2}$, $\Delta x = x_2 - x_1, \bar{t} = \frac{t_1+t_2}{2}$, $\Delta t = t_2 - t_1$ and setting the average position to zero we get:

$$V(x,t) = \sum_{i=1,2} \exp\left(-\frac{\left(x-(-1)^i\Delta x/2\right)^2}{2\sigma_x^2} - \frac{\left(t-(\bar{t}+(-1)^i\Delta t/2)\right)^2}{2\sigma_t^2}\right)$$

To calculate the time at which the wave passes through the midpoint between Gaussians, we calculate the temporal derivative at x=0 and equate it to zero. This yields the following relation which is satisfied at $t = \bar{t}$.

$$\frac{\left(t-(\bar{t}-\Delta t/2)\right)}{\left(t-(\bar{t}+\Delta t/2)\right)} = -\exp\left(\frac{\Delta t(t-\bar{t})}{\sigma_t^2}\right)$$

To track the wave front's peak, we calculate the spatial extremum by equating the first spatial derivative to zero at $t = \bar{t}$.

$$\frac{(x+\Delta x/2)}{(x-\Delta x/2)} = -\exp\left(\frac{x\Delta x}{\sigma_x^2}\right)$$

This equation is satisfied at x=0. We calculate the second derivative to determine whether the extremum is concave or convex.

$$\left.\frac{\partial^2 V}{\partial x^2}\right|_{t=\bar{t},x=0} = \frac{2}{\sigma_x^2}\exp\left(-\frac{(\Delta x/2)^2}{2\sigma_x^2} - \frac{(\Delta t/2)^2}{2\sigma_t^2}\right)\left(\frac{1}{\sigma_x^2}(\Delta x/2)^2 - 1\right)$$

Since the sign of this expression depends only on the last multiplicand, we conclude that the extremum at $t = \bar{t}, x = 0$ will be a maximum when $\Delta x < 2\sigma_x$ and a minimum for when $\Delta x > 2\sigma_x$.

Similarly to the spatial domain, we can calculate the conditions for identifying two Gaussians over the temporal domain. We require that no minimum appears at x=0 during the period between the two peaks reaching their maximum. i.e., $\forall t \in (t_1, t_2)$, $\frac{\partial^2 V}{\partial t^2}(x=0,t) \leq 0$. This results in the following equation:

$$\frac{\left(\left(t-\left(\bar{t}-\frac{\Delta t}{2}\right)\right)^2 - \sigma_t^2\right)}{\left(\left(t-\left(\bar{t}+\frac{\Delta t}{2}\right)\right)^2 - \sigma_t^2\right)} \leq -\exp\left(\frac{(t-\bar{t})\Delta t}{\sigma_t^2}\right)$$

By separately considering the case of $t \geq \bar{t}$ and $t < \bar{t}$, one can show that:

$$(t-\bar{t})^2 + \left(\frac{\Delta t}{2}\right)^2 \leq \sigma_t^2 \quad \forall t \in (t_1, t_2)$$

Plugging in t=t_1 or t=t_2 (in which the left hand side is maximal) yields a tight bound of $\Delta t \leq \sqrt{2}\sigma_t$.

To calculate the velocity profile of the peak, we find $\frac{\partial V}{\partial x}$ and equate it to zero. This yields the following relation between x_p and t , depicting the coordinates in which the profile is at its peak:

$$\left(x_p + \frac{\Delta x}{2}\right)\exp\left(-\frac{x_p \Delta x}{\sigma_x^2} + \frac{\Delta t(\bar{t} - t)}{\sigma_t^2}\right) = -\left(x_p - \frac{\Delta x}{2}\right)$$

From this equation, one can isolate t = g(x_p)

$$\bar{t} - \frac{\sigma_t^2}{\Delta t}\ln\left[-\frac{\left(x_p - \frac{\Delta x}{2}\right)}{\left(x_p + \frac{\Delta x}{2}\right)}\right] - x_p \frac{\Delta x}{\Delta t}\frac{\sigma_t^2}{\sigma_x^2} = \mathrm{t}$$

From this equation we calculated $\frac{dt}{dx_p}$, and under the condition that $\Delta x < 2\sigma_x$, we can use the inverse function theorem to get $\frac{dx_p}{dt}$:

$$\frac{dx_p}{dt} = \frac{\Delta t}{\sigma_t^2} \cdot \frac{\sigma_x^2 \Delta x}{4\sigma_x^2 - \Delta x^2}$$

A similar approach was taken for calculating the velocity of the peak for an oscillating sources model:

$$V(x,t) = \sum_{i=1,2} \cos(2\pi f t - \phi_i) \cdot \exp\left(-\frac{(x - x_i)^2}{2\sigma_x^2}\right)$$

To calculate the peak velocity, we change coordinates to $\bar{x} = \frac{x_1 + x_2}{2}$, $\Delta x = x_2 - x_1, \Delta\phi = \phi_1 - \phi_2$, and equate the spatial derivative to zero:

$$\frac{\partial V}{\partial x} = -\frac{1}{\sigma_x^2}\sum_{i=1,2} \cos(2\pi f t - \phi_i) \cdot \left(x - (-1)^i \frac{\Delta x}{2}\right)\exp\left(-\frac{\left(x - (-1)^i \frac{\Delta x}{2}\right)^2}{2\sigma_x^2}\right) = 0$$

Giving rise to the condition:

$$\frac{\cos(2\pi f t - \phi_1)}{\cos(2\pi f t - \phi_2)} = -\frac{\left(x - \frac{\Delta x}{2}\right)}{\left(x + \frac{\Delta x}{2}\right)} \exp\left(\frac{x\Delta x}{\sigma_x^2}\right)$$

We next calculate the partial derivative with respect to t, to get:

$$\frac{dx}{dt} = 2\pi f \sin(\Delta\phi) \cdot \frac{\sigma_x^2\left(x + \frac{\Delta x}{2}\right)^2}{\Delta x\left(x^2 + \sigma_x^2 - \left(\frac{\Delta \mathrm{x}}{2}\right)^2\right)\exp\left(\frac{x\Delta x}{\sigma_x^2}\right)}$$

For examining phase latency maps under different spatially distributed Gaussians, we used a simplistic representation in which two 2D spatial gaussians were each multiplied by a temporal squared sine:

$$V(x,y,t) = \sum_{i=1,2} w(t-t_i)\sin^2(t-t_i)\exp\left(-\frac{(x-x_i)^2+(y-y_i)^2}{2\sigma_i^2}\right)$$

where $w = \Theta(t)\Theta(\pi - t)$ is a window function (Θ is the Heavyside step function) and t_i is the time in which pulse i starts. For generating phase WLPs with different spatial arrangements, we used the following parameters. Plane wave: $t_1 = 1; t_2 = 30$ (70% temporal overlap); $(x_1, y_1) = (3,3)$; $(x_2, y_2) = (9,9)$; and $\sigma_1 = \sigma_2 = 6$; $\Delta x = \sqrt{2}\sigma$. Radial wave: $t_1 = 1; t_2 = 30$; $(x_1, y_1) = (x_2, y_2) = (3,3)$; $\sigma_1 = 3$; $\sigma_2 = 6$. For the spiral-like wave we used two Gaussians with non-zero covariance:

$$V(\vec{X},t) = \sum_{i=1,2} w(t-t_i)\sin^2(t-t_i)\exp\left(-\frac{1}{2}\left(\vec{X}-\vec{X_i}\right)^T\Sigma_i^{-1}\left(\vec{X}-\vec{X_i}\right)\right)$$

with $\vec{X}$ being the spatial coordinates, $\vec{X}_i$ the center of the i'th Gaussian and Σ_i is its covariance matrix. Parameters were $t_1 = 1$; $t_2 = 30$; $\vec{X}_1 = (8,4)$; $\vec{X}_2 = (8,8)$; $\Sigma_\mathrm{i} = R^{-1}(\alpha_i)GR(\alpha_i)$ where $R = \begin{pmatrix}\cos(\alpha) & -\sin(\alpha)\\ \sin(\alpha) & \cos(\alpha)\end{pmatrix}$ is the rotation matrix, $G = \begin{pmatrix}8 & 0\\ 0 & 15\end{pmatrix}$ is the covariance matrix of a vertical elliptical Gaussian, and $\alpha_{1,2} = \pm\frac{\pi}{4}$.

EEG Simulations. Simulations were performed using Brainstorm (version 3.220616) in Matlab [50]. Electrical field and consequent EEG recordings flowing defined activation profiles were simulated based on a human anatomical MRI scan. Activity sources were synchronized groups of dipoles located at the cortex surface and oriented normally to it. These grouped dipoles (red and blue dots in Figure 1b) are called scouts in the Brainstorm jargon and were manually marked on the cortical surface using the Brainstorm GUI. Each scout is comprised of 160 adjacent dipoles and has an average area of 27 cm^2 (20 dipoles of area 0.187cm^2 for small scouts). In each simulation, two scouts were activated with the same temporal Gaussian function (amplitude 1; standard deviation (sd) 0.2 seconds). This Gaussian was repeated consecutively five times with a period of 8sd, simulating activity for 9.66 seconds (5800 samples; 600Hz sampling rate). To simulate activation lags between modules (as in Figure 1), the temporal mean of one of the scouts was shifted by 0.2sd in every independent simulation, resulting with temporal differences ranging from 0.2sd to 2sd. In the same fashion, we repeated the simulation for varying spatial distance between the scout's centers (along the posterior-anterior axis) divided by the standard deviation. The distances were the Euclidean distance between the scouts' centers (mean position of each scouts' dipoles), and the standard deviation was calculated along the posterior-anterior axis for each scout (the mean of the two scouts was taken as the final value). In Brainstorm we used the default MRI anatomy (ICBM_152), with 15002 vertices (or 306716 for small scouts) and the "ICBM152" -> "ACA 10-05 343" EEG headset device (with 343 electrodes). We only analyzed the activity of the top 63 electrodes (35 for small scouts) at the vicinity of the sources. In the small scouts simulation (Fig S1a,b), we duplicated the sources such that they are symmetric across the two hemispheres. We modeled the electromagnetic properties of the head and the EEG device (forward

model) using the OpenMEEG BEM method [51,52] without inserting noise to the process (identity noise covariance matrix).

Results

Travelling waves are commonly reported in EEG recordings [3] but the cortical activations profiles underlying these waves remain unclear. We used simulations to test if sequential but spatially stationary activations can appear as travelling waves in EEG recordings. Specifically, we simulated the sequential activation (with time delay of ΔT) of two separate cortical areas in the parietal lobe (Figure 1a) and calculated the scalp EEG signals emanating from these activations using a forward model implemented in "brainstorm" [50] (Methods). We modeled signal sources in each area as a set of randomly distributed and periodically activated dipoles (Figure 1a).

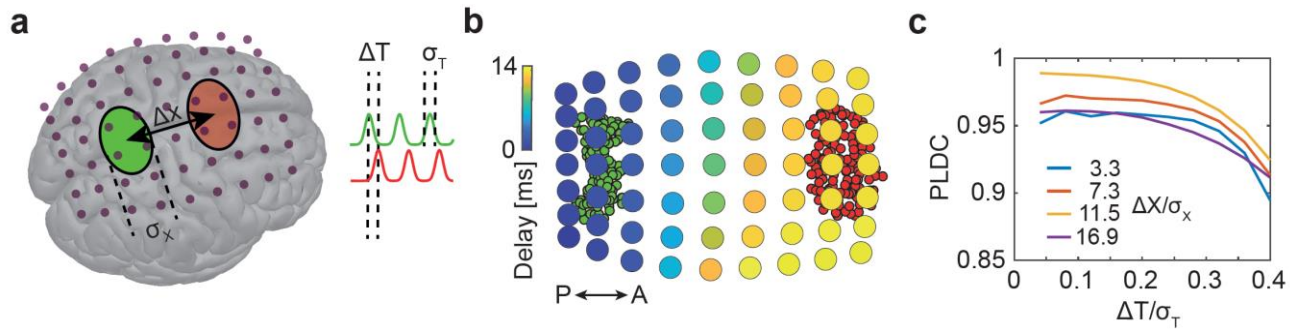

Figure 1. Sequential activation of two discrete brain areas appears as waves in simulated EEG phase latency maps. (a) Schematic illustration of simulated EEG. Two brain areas (green and red ellipses) are defined on the cortex by a set of dipoles that are activated uniformly with a time delay (ΔT) between areas. A finite element forward model in Brainstorm [50] is used to simulate the resulting potentials measured with EEG electrodes (purple dots). (b) Latency to peak measured across electrodes following the sequential activation of two sets of dipoles (green and red circles in the background) with a distance of 11cm ($\Delta x/\sigma_x$=16.9) and time delay of 20ms ($\Delta T/\sigma_T$=0.2). A continuous delay patterns propagating from posterior (P) to anterior (A) is observed. (c) Phase-latency distance correlations (PLDC) for different distances and different delays between two activated areas. PLDC remains close to 1 (indicating apparent wave propagation) for a wide range of values.

We first calculated the phase latency of the EEG signals across electrodes (Figure 1b). Interestingly, we observed a continuous range of delays gradually increasing along the anterior-posterior axis. Thus, phase delays did not reflect the modular construction of two spatially restricted sources. Rather, continuous propagation was observed for both large (Figure 1b) or small sources (Figure S1a,b). A standard approach for quantifying the existence of travelling waves is computing phase latency-distance correlation (PLDC) [2,10,12,53] which is the linear correlation between a defined phase crossing time (e.g., peak time) and the spatial location along the wave's trajectory. Applying this calculation to the data in Figure 1b along the posterior-anterior axis resulted in a value of 0.98, indicative of wave propagation. We next examined if such wave-like patterns (WLPs) are also detected if the distance between areas or the time delay between activations changes. Repeating the simulations for a range of distances and delays (Figure 1c) revealed high PLDC values in all distances which only slowly decay with

time delay. Furthermore, filtering the measured EEG signals with a narrow band filter (a common practice when analyzing specific oscillatory bands [3,4]) further increased PLDC (Figure S1c,d). These results suggest that detection of WLPs following sequential activation of spatially localized modules is abundant across parameters.

Our next aim was to capture the basic activity properties following the sequential activation of two discrete regions, using a simple analytical model. We assumed that the potential $V(x,t)$ is the sum of two one-dimensional Gaussians centered at x_1 and x_2 (with standard deviation σ_x), each multiplied by a temporal Gaussian centered around t_1 and t_2 (with standard deviation σ_t), respectively:

$$Equation\ 1 \qquad V(x,t) = \sum_{i=1,2} exp\left(-\frac{(x-x_i)^2}{2\sigma_x^2} - \frac{(t-t_i)^2}{2\sigma_t^2}\right)$$

In this model, the degree of signal spread (e.g. the electric field dispersion in EEG) can be modeled by changing the spatial Gaussian width, σ_x. The dynamics of these Gaussians for $x_2-x_1=\sigma_x=\sigma_t=1$ and $t_1=-1$, $t_2=1$ is plotted in Figure 2a. For these values, the two sequentially activated Gaussians are characterized by a WLP whose peak moves from point $x_1=-0.5$ to $x_2=0.5$. Importantly, this moving peak is always concave (Figure 2b-yellow curve). As the distance between Gaussians ($\Delta x=x_2-x_1$) increases, this WLPs will look more like two discrete events and for large enough distances the peak will be replaced by a minimum (Figure 2b – blue curve), spatially separating the two Gaussians (Supplementary Video 1). To calculate the condition distinguishing between these two scenarios, we calculated the position of the propagating peak by equating the spatial derivative of Equation 1 to zero (Figure 2c – black line, Methods). The concavity of the propagation profile can be determined by calculating the sign of the second spatial derivative at x=0 and $\bar{t}=(t_1+t_2)/2$. For $\Delta x<2\sigma_x$, this sign in negative (Methods) indicating that V(x) has a concave propagating peak which does not allow identifying two Gaussian peaks. This result is consistent with calculated PLDC values which are very high for $\Delta x<2\sigma_x$ (Figure 2i). Even for $\Delta x>2\sigma_x$, when $V(x)$ has a convex center point (Figure 2b-blue trace), PLDC values remain high suggesting that the values of PLDC may not be a good metric for detecting waves under these conditions. Temporal considerations can also be important for understanding the propagating maximum's dynamics. Calculating the peak dynamics at x=0 at times surrounding $\bar{t}$ shows that as long as the Gaussians are sequentially activated within a time frame of $\Delta t = \sqrt{2}\sigma_t$ the maximum has a single temporal peak (see Methods).

Given the wide range of travelling wave velocities in the literature, we calculated the velocity of WLPs' peak, v_p, and examined how it varies with model parameters under the condition of $\Delta x<2\sigma_x$ (Methods). This derivation reveals that the velocity is maximal at $x=0$, and at that point can be described by the following equation (Methods):

$$Equation\ 2 \qquad v_p = \frac{dx_p}{dt} = \frac{\Delta t}{\sigma_t^2} \cdot \frac{\sigma_x^2 \Delta x}{4\sigma_x^2 - \Delta x^2}$$

At small distances $\Delta x \ll \sigma_x$, the velocity linearly grows with distance between gaussians (Δx). Interestingly, as Δx grows towards the value $2\sigma_x$, propagation velocity sharply increases (Figure 2d). In contrast, when the temporal overlap between the two Gaussians increases (Δt decreases or σ_t increases), the velocity decreases with a stronger contribution of σ_t. Thus, propagation velocity can vary depending on the distances between activated areas, their standard deviation and the activation delay.

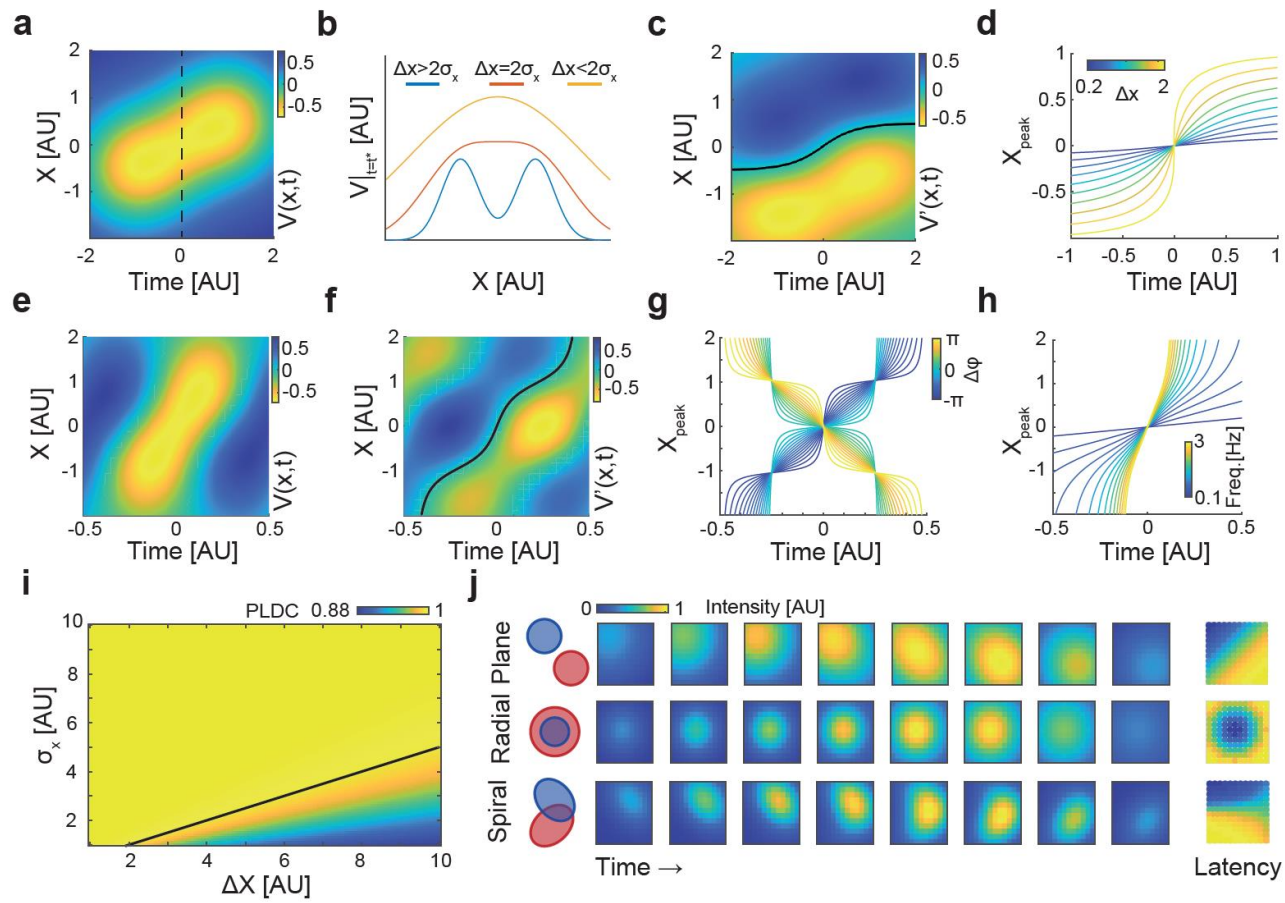

Figure 2. A simple analytic model of sequentially activated Gaussians exhibits travelling peaks with a diversity of patterns. (a) The spatiotemporal potential of two sequentially activated one dimensional spatial Gaussians (centers; x_1=-0.5 and x_2=0.5; standard deviation σ_x=1), each with a temporal Gaussian activation profile (peaking at t_1=-1 and t_2=1; standard deviation σ_t=1), as in Equation 1. Notice wave-like propagation. (b) Spatial profile of Equation 1 at time $\bar{t}=(t_1+t_2)/2$ (dotted line in (a)) for 3 conditions. Notice that for $\Delta x \leq 2\sigma_x$ the spatial profile is a concave. (c) The spatial derivative of V(x,t) in (a). Black line marks Gaussian peak dynamics (zero crossing points of the spatial derivate). (d) Peak dynamics for different values of distances between Gaussian centers (Δx). Notice that the average velocity increases with Δx. (e,f) Same as in (a,c) but for a model of a periodically fluctuating Gaussian (Equation 3) (x_1=-0.5, x_2=0.5, σ_x=1, f=1, $\phi_1=-3\pi/8$, $\phi_2=3\pi/8$).(g,h) The peak dynamics (as in d) for the model in (e,f) as a function of the phase difference between Gaussians, $\Delta\phi$ (g), and f, the frequency of the oscillation (h). f=1 in (g) and $\phi_1=-\pi/4$, $\phi_2=\pi/4$ in (h). Notice that wave velocity increases with frequency and can changes sign as a function of $\Delta\phi$. (i) PDLC values calculated for different Δx and σ_x. Black line marks the $\Delta x=2\sigma_x$ border. (j) Plane, radial and spiral-like propagation patterns and the resulting phase latency maps (right) for different spatial arrangements of two sequentially activated Gaussians (left).

Travelling waves are often reported as propagating phase delays when tissue excitability is oscillatory [3,4]. We therefore examined the spatiotemporal dynamics of two Gaussians with a temporal periodic activation profile with frequency f and phase delay ϕ between sources:

$$Equation\ 3 \qquad V(x,t) = \sum_{i=1,2} cos(2\pi f t + \phi_i\ )exp\left(-\frac{(x-x_i)^2}{2\sigma_x^2}\right)$$

Similarly to the temporal Gaussian model, the periodic model exhibits a WLP with a travelling maximum (Figure 2e). Calculating the propagation velocity of the wave's peak (Figure 2f – black line) results in the following relation (Methods):

$$Equation\ 4 \qquad v_p = 2\pi f \sin(\Delta\phi) \cdot \frac{\sigma_x^2\left(x+\frac{\Delta x}{2}\right)^2}{\Delta x\left(x^2+\sigma_x^2-\left(\frac{\Delta x}{2}\right)^2\right)\exp\left(\frac{x\Delta x}{\sigma_x^2}\right)}$$

This equation reveals two interesting properties: First, the sign of the peak's velocity, v_p, depends on the phase difference between the two Gaussians ($\Delta\phi=\phi_2-\phi_1$). Thus, the peak can travel either forward or backward following small changes in phase delays (Figure 2g). Second, the position of the peak (Figure 2h), and therefore the propagation speed (Equation 4), is proportional to the oscillation frequency. Thus, faster oscillations propagate at higher velocities in this model.

The spatial activation spread (σ_x) of a cortical module can result from the measurement techniques (due to passive conductance) but also from the spatial organization of inputs and outputs patterns and their associated synaptic currents. We hypothesized that changing these patterns can produce different phase latency maps. We therefore extended the periodic model in Equation 3 to two dimensions (Methods) and to Gaussians with different shapes (different covariance functions) (Figure 2j). When sequentially activated Gaussians had been placed one next to the other ($\Delta x=\sqrt{2}\sigma_x$) their propagation patterns and phase latency map resembled a plane wave (Figure 2j-top). When Gaussians overlap spatially, with the first Gaussian having a smaller σ, their sequential activation resembled a radial wave (Figure 2j-middle). Interestingly, calculating PLDC, which was developed to discriminate between a radial wave and a bump with increasing amplitude [2], resulted in a value of 0.92, indicative of a travelling wave. Finally, by positioning two Gaussians with one longer axis such that their major axes are perpendicular to one another, a pattern with features of a spiral-like wave was observed (Figure 2j-bottom). These examples illustrate that using a combination of only two sequentially activated Gaussians, a wide range of phase latency profiles corresponding to plane, radial and spiral-like waves could be generated. We note that while we used simple activation profiles, spatial modules in brains (e.g., cortical columns or spatially localized projection patterns) can be more diverse and potentially facilitate a large repertoire of phase latency patterns which, despite being seemingly discrete, might be classified as travelling waves.

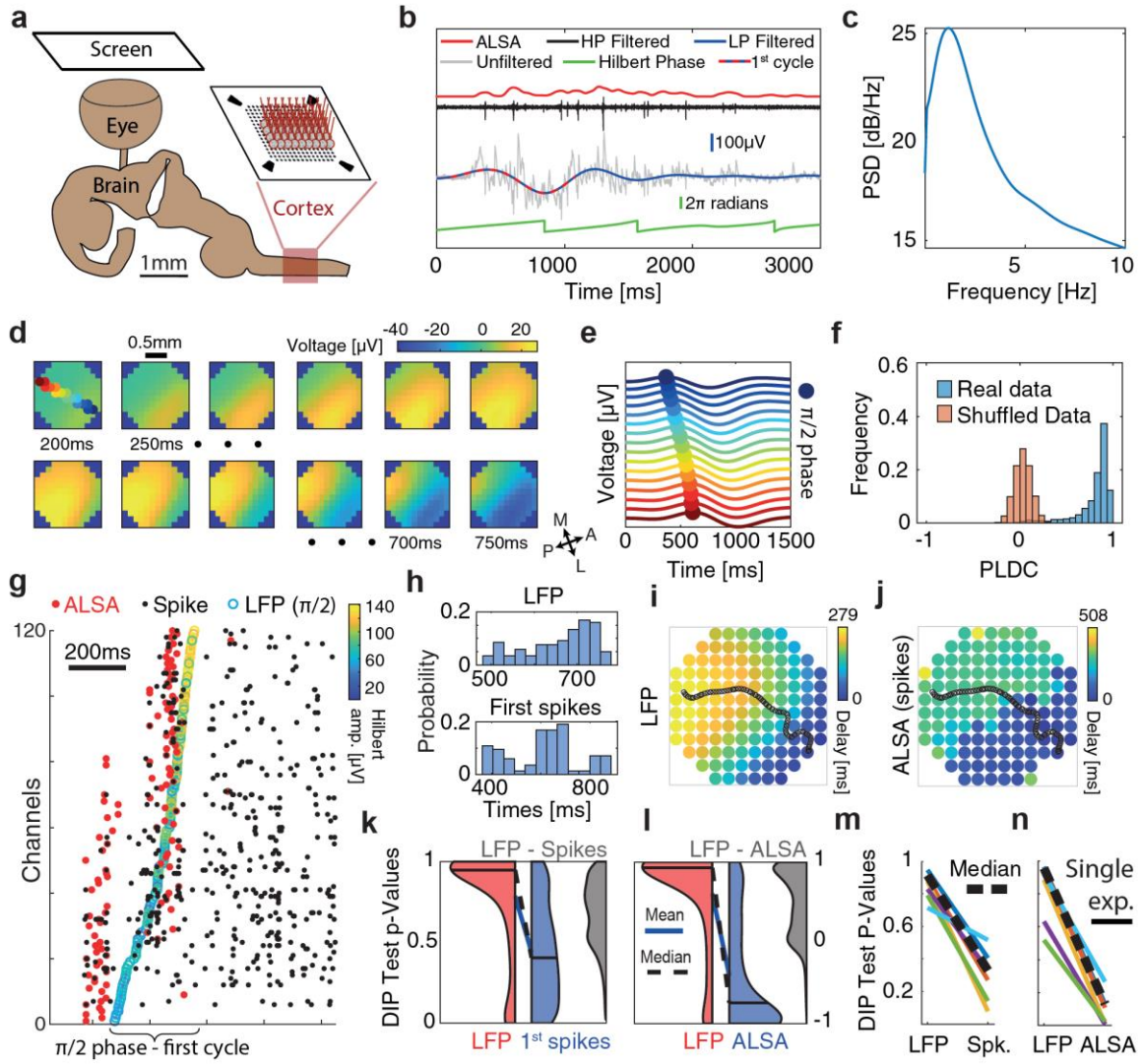

Figure 3. Sequential activation of discrete spiking populations underlies LFP waves in turtle cortex. (a) Schematic of the experimental setup. The brain with eye attached is extracted and the visual cortex is flattened on a MEA and its activity is measured in response to visual stimulation of the retina. (b) A cortical response following visual stimulation at t=0. Traces show the following data: raw electrode (grey), low-pass filtered (<2Hz, blue with dotted line marking the first oscillation cycle), high-pass filtered (>200Hz, black), ALSA (red) and the instantaneous phase of the low-pass filtered trace (green). (c) Power spectral density (averaged over 1000 randomly selected trials from one experiment). (d) Dynamics of low-pass filtered (<2Hz) and averaged (n=4000) cortical responses to visual stimulation. Amplitude in each time window (200-750ms post stimulus in 50ms intervals) is color coded and presented on the physical space of the electrode. Filled color-coded circles mark the electrodes recorded in (e). M=Medial, A=Anterior, L=Lateral, P=Posterior. (e) Averaged (n=4000) low-pass filtered (<2Hz) traces for channels along the delay gradient. The maximum is marked by a circle and its location on the array is color coded in (d). (f) Phase Latency-distance correlation (PLDC) distribution for all trials with strong waves (n=2415, blue) from this experiment and for the same trials with shuffled latencies (red). (g) Spiking responses (black dots) in a single visual stimulation trial. Empty circles mark the π/2 phase crossing. Red circles denote the ALSA onset for each electrode. Electrodes were reordered according to the LFP phase crossings. (h) The distribution of LFP phase crossing times and first spike times for the response in (g) with corresponding DIP values (0.85 and 0.0002, respectively). (i-j) Latency maps on the electrode array's physical space extracted from the Hilbert phase (i) and ALSA (j). Black line denotes the wave center path extracted from the Hilbert phase (see Methods). (k) DIP-test p-value distribution of the 1st spikes (blue), Hilbert phase crossings (red) and differences between both per trial (gray) for strong waves with enough spikes (n=902). Distribution medians (solid black line) are connected by a dashed black line (blue line connects the distributions' means). (l) Same as (k) but for ALSA. (m,n) Medians of the DIP-test p-values (black lines in k,l, respectively) from 6 recordings in 4 animals. Dashed black line marks the median over all experiments. All results except (m,n) are from the same recording.

Our next aim was to examine whether WLPs exist in cortical tissue. To do this, one needs a system with identified travelling waves across cortex, in which we can measure the microscopic tissue supra-threshold excitability, i.e., spikes, across cortex. To achieve such measurements, we utilized the ex-vivo eye-brain turtle preparation [47]. In this preparation (Figure 3a), the whole brain with the eye attached is extracted, and the dorsal cortex - a three layered homolog of the mammalian cortex [54] - is flattened onto a multi electrode array (MEA). The advantage of this preparation is that it allows large-scale two-dimensional (in directions tangential to the cortical surface) sampling of both spiking and LFP activity. Furthermore, previous works with this preparation have shown the existence of waves that travel across cortex following visual stimulation [11,46].

Corresponding with previous reports [55], visual stimulation elicited increases in LFPs and spikes (Figure 3b – gray and black traces respectively) across large regions of the visual cortex. Although responses varied in intensity between stimulations, they typically started ~200ms post-stimulus and lasted for ~2 seconds. Spectral analysis revealed that responses were characterized by high power at low frequencies (Figure 3c). Specifically, applying a 2Hz low-pass filter captured the strong fluctuations in LFP following visual stimulations (Figure 3b – blue trace). We next set to examine how this low frequency band propagates across cortex. Averaging over all trials revealed a clear propagation pattern travelling from anterolateral to posteromedial (Figure 3d). This pattern was consistent with previous reports of waves travelling from area D2 to area D1 in turtle cortex [11]. To illustrate this propagation on the time domain, we plotted the first oscillation cycle of the filtered LFP (2Hz lowpass, Figure 3b – red and blue dotted line) along a linear wave path (Figure 3e). The maximum showed a clear propagation pattern with a velocity of 1.8±0.35mm/s (mean$\pm$std).

To quantitatively estimate the propagation trajectories during single oscillations cycles, we used the analytic signal of the Hilbert transform [9,18,56] (Methods). We first identified the $\pi/2$ phase crossing times of all oscillation cycles. We then grouped phase crossings into events belonging to single oscillation cycles based on continuity of phases across space and time (Methods, Figure S2). The first oscillation cycle showed a clear propagating wavefront, but more importantly, intense spiking activity. We therefore focused our analysis on this cycle and calculated the propagation direction of this cycle. To do so, we defined the wave center path, as the weighted spatial center of mass of all the channels' phase crossings for a given time point with weights given by the amplitude of the Hilbert envelope (Methods). Examining phase delays and the wave center path for a single trial (Figures 3i) revealed a pattern that resembled the averaged propagation (Figure 3d) but varied between trials (Figure S3). We next calculated the PLDC values for the first oscillation cycle in response to visual stimulation across all trials and plotted their distribution (Figure 3f-blue). PLDC values were close to 1 suggesting the existence of propagating waves. For comparison, calculating PLDC after shuffling the channels' phase latencies dramatically reduced PLDC to an average close to zero (Figure 3f-red).

To examine whether local spike dynamics propagated continuously across space as the LFP, we examined the timing of the first spikes (marking the onset of excitability) during the first oscillation cycle of the filtered LFP. Spikes were generally locked to the LFP oscillation with a peak spiking rate at a phase of 0.53π (Figure S4a). To compare the spatiotemporal spiking patterns with the LFP patterns, we reordered the recorded electrodes according to the $\pi/2$ Hilbert phase. As expected, phase gradually advanced across electrodes (Figure 3g – empty circles). In contrast, spiking activity was not continuous

over space but clustered in discrete temporal bouts (Figure 3g – black dots). To quantify this clustering in spike times, we assigned the neurons to channels according to their maximal amplitude channel and used the DIP-test to quantify temporal statistics [49]. The DIP-test measures the deviation of a distribution from unimodality and could well capture the differences in spike and LFP onsets. The LFP phase crossings were temporally continuous and therefore did not strongly deviate from a uniform distribution (Figure 3h, p-value 0.85). In contrast, spike timings were segregated into temporal groups and were not unimodally distributed (p-value < 0.0002). We applied this test on the first oscillation cycles across trials (Figure 3k). Since not all channels had active spikes in all trials, we ran the DIP test (for both spikes and LFP) only on the subset of channels with spikes within each trial. The results showed a consistently larger DIP for spikes vs. LFP (Figure 3k – red vs blue areas). This difference was not only significant on the average level but was also evident when comparing the P-value of pairwise differences calculated for each trial separately (Figure 3k – grey area). Finally, repeating this analysis for recordings in other animals reveal consistent results (Figure 3m), indicating that while LFP activity along the wave path resembles a continuously propagating wave, the spiking activity – a marker of local excitability - is more consistent with sequentially-activated spatially-segregated modules.

The above analysis was limited to the subset of channels with spikes within the first cycle in every trial. To examine propagation wavefronts across a larger fraction of channels, we constructed a more robust estimate of local spiking excitability. Specifically, we calculated the Average Local Spiking Activity (ALSA), which is the weighted average of each channel's spiking rate with its nearest neighbors' spiking rates (Methods). The spiking onset time for each channel was defined as the time of the first maximum of the ALSA (Figure 3b-red curve, 3g-red dots). Since many neurons did not exhibit spiking activity during the wave onset (e.g., Figure 3g illustrates how for some channels, the first spikes in a cycle occur long after the activation has reached nearby channels), this measure allows estimating the wavefront propagation across many channels. Correspondingly, the ALSA phase distribution resembled that obtained with single spikes but was more sharply locked to the LFP oscillation phase (Figure S4b). Comparing ALSA with LFP revealed stronger differences between spikes and LFP. In contrast to the LFP (Figure 3i, S5a-c), the ALSA onset times did not evolve continuously across space but were organized in two separate and sequentially activated spatial groups (Figure 3j, S5d-f). Comparing the DIP test for LFP and ALSA revealed a consistent difference across trials in both the average DIP values as well as the difference in single trials (Figure 3l) that replicated over experiments (Figure 3n). We note that we focused the above analysis on waves in the low frequency LFP band (0-2Hz) because these events recruited enough spikes to analyze their phase relations. However, propagating patterns were also detected in other frequency bands (Figure S6) and showed complex patterns including plane waves, radial waves and spiral waves.

Discussion

In this work we investigated the link between electrophysiological measurements of travelling waves and their underlying neuronal activations. To do so, we used common approaches for detecting travelling waves in neural data at different scales and contrasted these results with ground truth neural excitability. We showed that LFP measurements indicative of waves propagating across turtle cortex

are underlined by discrete and consecutively activated neuronal populations, and not by a continuously propagating wavefront of spikes (Figure 3). Similarly, activation profiles that resemble continuous travelling waves in EEG simulations can be underlined by consecutive activation of two discrete cortical regions (Figure 1). We replicated these results using an analytical model and demonstrated that a simple scenario of sequentially activated Gaussians can exhibit WLPs with a rich diversity of spatiotemporal profiles (Figure 2). Our results offer insight into the scenarios and conditions for WLP detection by identifying failure points that should be considered when identifying travelling waves and therefore suggest caution when interpreting continuous phase latency maps as microscopically propagating wave patterns. Further, our results suggest that the discrepancy between modular and wave activation should be examined across spatial scales. Thus, it is not necessarily the case that at the fine grained (single neuron) scale activation patterns are modular, but, following coarse graining, smooth wave patterns emerge. Rather, modular activation may hierarchically exist across scales [24,57] and may be masked by smeared spatial supra-threshold excitability boundaries. Below we discuss these limitations across techniques and their implications.

Our analytical results suggest that the main parameter affecting the detection of WLPs in a sequentially activated modular system is the distance between modules relative to their spatial spread. In contrast to the distance between modules, the spatial spread can be strongly affected by the experimental approach used for measurements. For potential-based measurements, the spread will markedly increase with medium conductance and distance from the source, as predicted from the volume conductance theory [36]. Our simulations show that spatial spread will be large in EEG measurements (Figure 1) where the distance between the sources and the electrodes is large, and the skull and meninges disperse the electrical field generated by localized cortical currents [37,58]. Dispersion can also be substantial in intracranial measurements such as ECoG due to the high conductivity of the cerebro-spinal fluid [36,38]. Interestingly, large spread was also observed in our MEA LFP recordings, where no meninges separate between the electrodes and tissue. Further, the small distance between the tissue and the electrodes limits conductance through the artificial cerebro-spinal fluid. Despite this, propagation appeared spatially continuous in LFP, suggesting contributions from volume conduction through the tissue and non-local current sources, for example, activated synaptic terminals from axons of distant neurons. This spread is aligned with theoretical studies calculating spatial decay constants of hundreds of micrometers [59] and with experiments reporting contributions from sources millimeters away [37].

Travelling waves were also measured using VSD imaging [8,9,60,61], a method that does not suffer from passive electric field spread as it measures transmembrane potentials. However, light scatters in optical signals, especially in wide field imaging. More importantly, VSD measurements report subthreshold potentials integrating excitability from large areas due to synaptic currents originating from long distance neurons in addition to local ones [16,39]. Correspondingly, deflection of a single whisker results in cortical activation that extends beyond the corresponding barrel [15,16]. From measuring VSD alone, it is unclear which component of this extended signal reflects supra-threshold activation. If supra-threshold activity is mostly restricted to the barrel and the extended spread mostly reflects sub-threshold activity, sequentially activating two nearby whiskers will result in WLPs.

Similarly, sequential activation of two areas in visual space can appear to elicit a wave in the visual cortex, as observed for anesthetized cats [17].

Increased spatial spread and WLP may not only result from non-local measurement but also from data analysis. For EEG specifically, amplitudes are relatively small, and consequently waves are often reported using averaged data. In combination with the inherent variability in neuronal signals [62], averaging may smooth the boundaries between modules [63], effectively increase the spatial spread and therefore promote the identification of WLPs.

Such a spread may explain the smoother FLP profiles after averaging (Figure 3d) relative to single trials (Figure 3g,i) in turtle cortex. While modularity in turtle cortex connectivity structure was not systematically mapped, the temporal grouping of spike timings across two regions of turtle cortex (Figure 3i) is spatially aligned with structural transition between areas D1 and D2 [11,64]. This transition was not evident in the LFPs, possibly due to the longer decay constants of slow potentials and the existing connection between D2 and D1. Such connections elicit sub-threshold synaptic currents following D2 activations which can further contribute to LFP spread. Similarly, sequentially activating adjacent cortical regions, which are functionally correlated and structurally connected (e.g., as activity travels across visual regions from V1 to V4), may be activated in a modular fashion but identified as travelling in VSD signals [65] due to mesoscale connectivity [66,67]. However, this modularity would be harder to detect for fast waves (in contrast to the slow waves in turtle cortex). Monitoring wave dynamics at a single cell resolution across connectivity boundaries (e.g., across two adjacent cortical regions or column), will be instrumental in identifying the granularity of propagating patterns in other cortical regions.

In addition to spatial factors, temporal factors and analysis schemes may promote WLPs. Our analytical results suggest that a single maximum during dynamics will emerge when sequentially activated Gaussians considerably overlap in time ($\Delta t<\sqrt{2}\sigma_t$). Thus, discriminability between Gaussian activations will decrease with increase in σ_t, for example, following filtering. Indeed, filtering into narrow frequency bands is a common practice in EEG research and is bound to smooth sharp transients. Correspondingly, our EEG simulations indicate that filtering markedly increased PLDC (Figure S1c,d). We note that the detection of WLPs is not restricted to specific frequency bands; our simulation and analytic results are not band dependent. Our turtle data also contained waves in other bands (Figure 4S). The low spike rates in our preparation prevented us from performing a significant statistical analysis to compare these waves with underlying spiking patterns. Such examinations will be critical for understanding the propagation patterns of spikes during waves across multiple frequency bands. To do so, spatial characterization of single trials dynamics, rather than calculating average spiking locking across space [68], will be required.

Analysis techniques can potentially resolve the discrepancy between waves and modular activation for different levels of granularity. Phase latency maps and correlations are a valuable step towards differentiating between single stationary bumps and travelling waves [9] and continues to be used to date [3,12,69]. The underlying assumption of this approach is that a stationary bump is characterized by a flat latency map because every channel reaches its maximum at the same time, in contrast to increase in a particular direction, in case of a wave. However, this approach does not consider the possibility of

sequentially activated local populations. Indeed, our results show how activity profiles resulting from two sequentially activated Gaussians meet the phase latency conditions for waves. Developing good methods for separating travelling waves from WLPs will require validating these methods using experimental paradigms providing information about spiking activity across space. In addition, more frequent usage of available techniques to decrease the spread of signals and increase localization [70] will increase the separability between waves and modular activation.

Our results can explain some of the reported variability in travelling propagation directions and velocities [3]. We showed that the propagation direction of WLPs is determined by the location of sequentially activated modules (Figure 1) and the propagation speed of WLPs by the distance between modules and their temporal delay (Figure 2, Equation 2). In addition, when calculating propagation speeds for narrow-band signals, velocities increase linearly with frequency band and may even reverse direction as a function of the phase lag between oscillatory areas (Equation 4 and Figures 2e-h). These results are interesting given that cortical waves in the same tissue can propagate both in forward and backwards directions and that higher frequencies propagate faster [53,71,72]. Variability in propagation speed could also be detected when examining single oscillations in our turtle recordings (Figure S2 vs S6). The above results echo findings in a recent study showing that cortical responses to similar stimuli vary in propagation profile for EEG and MEG recordings and that this discrepancy can be accounted by modelling sequentially activated sources [44,73]. In general, variability in responses may also be explained by differences in propagation mechanisms [3,4,74], for example, waves in axonal collaterals [9] will travel faster relative to waves which propagate through single neuron excitability [75] and therefore better measurements of tissue excitability on a finer scale can resolve such discrepancies.

The above discussion calls for a better classification of dynamical phenomena into wave or modules. In some neural systems, wave activity patterns clearly dominate. A very prominent example is developing systems. Measurements from retinas ex-vivo were performed across large areas with single cell resolution using both calcium imaging and dense electrode arrays [43,76–78]. In such measurements, spatially adjacent neurons were shown to be activated sequentially in two-dimensional spreading patterns. Travelling waves were also detected in developing cortex, thalamus, and other brain areas [76,79].

In contrast, in mature circuits, and specifically in cortex, connectivity and possibly excitability profiles are replaced by modules and by segregated excitability [24,30,57,80]. Functional modular organization may result from control of neuronal excitability [31,57] in combination with modular connectivity patterns [24,30]. Accordingly, travelling waves may dominate in specific conditions of reduced consciousness such as anesthesia or sleep [3,5,6,81,82]. Interestingly, waves are also reported under pathological conditions such as epilepsy [83]. In such states, inhibition in the network is reduced [84] which may lead to a replacement of modular segregated activation by large-scale propagation of excitability crossing modular boundaries [31]. The abundance of travelling waves suggests that they are important components of the repertoire of neural network activity patterns. However, clear evidence for waves in some systems, for example during development, does not imply their existence in other systems. Indeed, wave propagation patterns on the single cell level are only scarcely reported during wakefulness [7,69] leaving the microscopic correlates of most travelling wave unknown.

A promising technique for mapping the dynamics of microscopic local excitability is Calcium imaging. The data provided by this method supports both localized sequential activations [85] as well as travelling motifs [85]. However, to the best of our knowledge, no analysis was performed to discriminate between waves and sequentially activated sources and syncs. In addition, the temporal resolution of Calcium imaging is low, making it hard to detect temporal boundaries, especially for fast oscillating waves (e.g., in the gamma range). Further, wide point spread functions, axonal projections, or sparse activation of adjacent populations and may mask circuit modularity and promote wave-detection [86]. On the other hand, the advancement of fast imaging techniques and analysis[87] in combination with cell-body-targeted Calcium indicators [88] and high optical sectioning methods chart a promising direction for systematic investigations into the granularity of propagating patterns in the brain. Such measurements together with new analysis approaches [89,90] will be required to disambiguate travelling waves from WLPs. Understanding the degree and the scale of functional modular organization in the brain will be important to revealing the true nature of cortical dynamics and its contribution to neural computations [3,91,92].

Acknowledgements

This project has received funding from the Joint NSFC-ISF Research Fund (grant No. 3430/20).

Ethics declaration

The authors declare no competing interests.

Data availability

The datasets generated and/or analyzed during the current study are available from the corresponding author on reasonable request.

References

1. Sato, T. K., Nauhaus, I. & Carandini, M. Traveling Waves in Visual Cortex. *Neuron* vol. 75 218–229 Preprint at https://doi.org/10.1016/j.neuron.2012.06.029 (2012).

2. Muller, L. & Destexhe, A. Propagating waves in thalamus, cortex and the thalamocortical system: Experiments and models. *J Physiol Paris* **106**, 222–238 (2012).

3. Muller, L., Chavane, F., Reynolds, J. & Sejnowski, T. J. Cortical travelling waves: Mechanisms and computational principles. *Nat Rev Neurosci* **19**, 255–268 (2018).

4. Wu, J. Y., Huang, X. & Zhang, C. Propagating waves of activity in the neocortex: What they are, what they do. *Neuroscientist* **14**, 487–502 (2008).

5. Xu, W., Huang, X., Takagaki, K. & Wu, J. young. Compression and Reflection of Visually Evoked Cortical Waves. *Neuron* **55**, 119–129 (2007).

6. Massimini, M., Huber, R., Ferrarelli, F., Hill, S. & Tononi, G. The sleep slow oscillation as a traveling wave. *Journal of Neuroscience* **24**, 6862–6870 (2004).

7. Lubenov, E. V. & Siapas, A. G. Hippocampal theta oscillations are travelling waves. *Nature* **459**, 534–539 (2009).

8. Senseman, D. M. Spatiotemporal structure of depolarization spread in cortical pyramidal cell populations evoked by diffuse retinal light flashes. *Vis Neurosci* **16**, 65–79 (1999).

9. Muller, L., Reynaud, A., Chavane, F. & Destexhe, A. The stimulus-evoked population response in visual cortex of awake monkey is a propagating wave. *Nat Commun* **5**, (2014).

10. Huang, X. *et al.* Spiral Wave Dynamics in Neocortex. *Neuron* **68**, 978–990 (2010).

11. Prechtl, J. C., Cohen, L. B., Pesaran, B., Mitra, P. P. & Kleinfeld, D. Visual stimuli induce waves of electrical activity in turtle cortex. *Proc Natl Acad Sci U S A* **94**, 7621–7626 (1997).

12. Muller, L. *et al.* Rotating waves during human sleep spindles organize global patterns of activity that repeat precisely through the night. *Elife* **5**, (2016).

13. Takahashi, K. *et al.* Large-scale spatiotemporal spike patterning consistent with wave propagation in motor cortex. *Nat Commun* **6**, (2015).

14. Reimer, A., Hubka, P., Engel, A. K. & Kral, A. Fast propagating waves within the rodent auditory cortex. *Cerebral Cortex* **21**, (2011).

15. Ferezou, I., Bolea, S. & Petersen, C. C. H. Visualizing the Cortical Representation of Whisker Touch: Voltage-Sensitive Dye Imaging in Freely Moving Mice. *Neuron* **50**, (2006).

16. Petersen, C. C. H., Hahn, T. T. G., Mehta, M., Grinvald, A. & Sakmann, B. Interaction of sensory responses with spontaneous depolarization in layer 2/3 barrel cortex. *Proc Natl Acad Sci U S A* **100**, (2003).

17. Jancke, D., Chavane, F., Naaman, S. & Grinvald, A. Imaging cortical correlates of illusion in early visual cortex. *Nature* **428**, 423–426 (2004).

18. Rubino, D., Robbins, K. A. & Hatsopoulos, N. G. Propagating waves mediate information transfer in the motor cortex. *Nat Neurosci* **9**, 1549–1557 (2006).

19. Goldman, S., Santelmann, W. F., Vivian, W. E. & Goldman, D. Traveling waves in the brain. *Science (1979)* **109**, 524 (1949).

20. Patten, T. M., Rennie, C. J., Robinson, P. A. & Gong, P. Human cortical traveling waves: Dynamical properties and correlations with responses. *PLoS One* **7**, (2012).

21. Alexander, D. M. *et al.* Traveling waves and trial averaging: The nature of single-trial and averaged brain responses in large-scale cortical signals. *Neuroimage* **73**, 95–112 (2013).

22. Hughes, J. R. The Phenomenon of Travelling Waves: A Review. *Clinical Electroencephalography* **26**, 1–6 (1995).

23. Ribary, U. *et al.* Magnetic field tomography of coherent thalamocortical 40-Hz oscillations in humans. *Proc Natl Acad Sci U S A* **88**, 11037–11041 (1991).

24. Meunier, D., Lambiotte, R. & Bullmore, E. T. Modular and Hierarchically Modular Organization of Brain Networks. *Front Neurosci* **4**, 11 (2010).

25. Sporns, O. & Betzel, R. F. Modular Brain Networks. *Annu Rev Psychol.* **67**, 613–640 (2016).

26. Harris, J. A. *et al.* Hierarchical organization of cortical and thalamic connectivity. *Nature 2019 575:7781* **575**, 195–202 (2019).

27. Hilgetag, C. C., O'Neill, M. a & Young, M. P. Hierarchical organization of macaque and cat cortical sensory systems explored with a novel network processor. *Philos Trans R Soc Lond B Biol Sci* **355**, 71–89 (2000).

28. Jia, X. *et al.* Multi-regional module-based signal transmission in mouse visual cortex. *Neuron* **110**, 1585-1598.e9 (2022).

29. Markov, N. T. *et al.* Weight Consistency Specifies Regularities of Macaque Cortical Networks. *Cerebral Cortex (New York, NY)* **21**, 1254 (2011).

30. Mountcastle, V. B. The columnar organization of the neocortex. *Brain* **120 (Pt 4**, 701–722 (1997).

31. Shein-Idelson, M., Cohen, G., Ben-Jacob, E. & Hanein, Y. Modularity Induced Gating and Delays in Neuronal Networks. *PLoS Comput Biol* **12**, (2016).

32. Martinet, L. E. *et al.* Human seizures couple across spatial scales through travelling wave dynamics. *Nature Communications 2017 8:1* **8**, 1–13 (2017).

33. Hindriks, R., van Putten, M. J. A. M. & Deco, G. Intra-cortical propagation of EEG alpha oscillations. *Neuroimage* **103**, 444–453 (2014).

34. Mak-McCully, R. A. *et al.* Distribution, amplitude, incidence, co-occurrence, and propagation of human K-complexes in focal transcortical recordings. *eNeuro* **2**, (2015).

35. Michel, C. M. & Murray, M. M. Towards the utilization of EEG as a brain imaging tool. *Neuroimage* **61**, 371–385 (2012).

36. Buzsáki, G., Anastassiou, C. A. & Koch, C. The origin of extracellular fields and currents-EEG, ECoG, LFP and spikes. *Nat Rev Neurosci* **13**, 407–420 (2012).

37. Kajikawa, Y. & Schroeder, C. E. How local is the local field potential? *Neuron* **72**, (2011).

38. Herreras, O. Local field potentials: Myths and misunderstandings. *Front Neural Circuits* **10**, 101 (2016).

39. Chemla, S. & Chavane, F. Voltage-sensitive dye imaging: Technique review and models. *J Physiol Paris* **104**, 40–50 (2010).

40. Stepanyants, A., Martinez, L. M., Ferecskó, A. S. & Kisvárday, Z. F. The fractions of short- and long-range connections in the visual cortex. *Proc Natl Acad Sci U S A* **106**, (2009).

41. Chemla, S. & Chavane, F. A biophysical cortical column model to study the multi-component origin of the VSDI signal. *Neuroimage* **53**, (2010).

42. Pál, I., Kardos, J., Dobolyi, Á. & Héja, L. Appearance of fast astrocytic component in voltage-sensitive dye imaging of neural activity. *Mol Brain* **8**, (2015).

43. Voufo, C. *et al.* Circuit mechanisms underlying embryonic retinal waves. *Elife* **12**, (2023).

44. Zhigalov, A. & Jensen, O. Perceptual echoes as travelling waves may arise from two discrete neuronal sources. *Neuroimage* **272**, 120047 (2023).

45. Orczyk, J. J., Barczak, A., Costa-Faidella, J. & Kajikawa, Y. Cross laminar traveling components of field potentials due to volume conduction of non-traveling neuronal activity in macaque sensory cortices. *Journal of Neuroscience* **41**, (2021).

46. Senseman, D. M. & Robbins, K. A. High-Speed VSD Imaging of Visually Evoked Cortical Waves: Decomposition Into Intra- and Intercortical Wave Motions. *J Neurophysiol* **87**, 1499–1514 (2002).

47. Shein-Idelson, M., Pammer, L., Hemberger, M. & Laurent, G. Large-scale mapping of cortical synaptic projections with extracellular electrode arrays. *Nat Methods* **14**, 882–890 (2017).

48. Brainard, D. H. The Psychophysics Toolbox. *Spat Vis* **10**, 433–6 (1997).

49. Hartigan, J. A. & Hartigan, P. M. The Dip Test of Unimodality. *The Annals of Statistics* **13**, (2007).

50. Tadel, F., Baillet, S., Mosher, J. C., Pantazis, D. & Leahy, R. M. Brainstorm: A user-friendly application for MEG/EEG analysis. *Comput Intell Neurosci* **2011**, (2011).

51. Gramfort, A., Papadopoulo, T., Olivi, E. & Clerc, M. OpenMEEG: Opensource software for quasistatic bioelectromagnetics. *Biomed Eng Online* **9**, (2010).

52. Kybic, J. *et al.* A common formalism for the integral formulations of the forward EEG problem. *IEEE Trans Med Imaging* **24**, (2005).

53. Zhang, H., Watrous, A. J., Patel, A. & Jacobs, J. Theta and Alpha Oscillations Are Traveling Waves in the Human Neocortex. *Neuron* **98**, (2018).

54. Tosches, M. A. *et al.* Evolution of pallium, hippocampus, and cortical cell types revealed by single-cell transcriptomics in reptiles. *Science (1979)* **360**, 881–888 (2018).

55. Prechtl, J. C., Bullock, T. H. & Kleinfeld, D. Direct evidence for local oscillatory current sources and intracortical phase gradients in turtle visual cortex. *Proc Natl Acad Sci U S A* **97**, 877–82 (2000).

56. le Van Quyen, M. *et al.* Comparison of Hilbert transform and wavelet methods for the analysis of neuronal synchrony. *J Neurosci Methods* **111**, 83–98 (2001).

57. Kaiser, M. & Hilgetag, C. C. Optimal hierarchical modular topologies for producing limited sustained activation of neural networks. *Front Neuroinform* **4**, 8 (2010).

58. Akalin Acar, Z., Acar, C. E. & Makeig, S. Simultaneous head tissue conductivity and EEG source location estimation. *Neuroimage* **124**, (2016).

59. Lindén, H., Pettersen, K. H. & Einevoll, G. T. Intrinsic dendritic filtering gives low-pass power spectra of local field potentials. *J Comput Neurosci* **29**, (2010).

60. Han, F., Caporale, N. & Dan, Y. Reverberation of Recent Visual Experience in Spontaneous Cortical Waves. *Neuron* **60**, 321–327 (2008).

61. Slovin, H., Arieli, A., Hildesheim, R. & Grinvald, A. Long-term voltage-sensitive dye imaging reveals cortical dynamics in behaving monkeys. *J Neurophysiol* **88**, 3421–3438 (2002).

62. Fox, M. D., Snyder, A. Z., Zacks, J. M. & Raichle, M. E. Coherent spontaneous activity accounts for trial-to-trial variability in human evoked brain responses. *Nat Neurosci* **9**, 23–25 (2006).

63. Mouraux, A. & Iannetti, G. D. Across-trial averaging of event-related EEG responses and beyond. *Magn Reson Imaging* **26**, (2008).

64. Desan, P. H. The organization of the cerebral cortex of the pond turtle, pseudemys scripta elegans. *ProQuest Dissertations and Theses* (1984).

65. Gu, Y. *et al.* Brain Activity Fluctuations Propagate as Waves Traversing the Cortical Hierarchy. *Cerebral Cortex* **31**, (2021).

66. Yan, M. *et al.* Mapping brain-wide excitatory projectome of primate prefrontal cortex at submicron resolution and comparison with diffusion tractography. *Elife* **11**, (2022).

67. Oh, S. W. *et al.* A mesoscale connectome of the mouse brain. *Nature* **508**, 207–214 (2014).

68. Ray, S. & Maunse ll, J. H. R. Network rhythms influence the relationship between spike- triggered local field potential and functional connectivity. *Journal of Neuroscience* **31**, (2011).

69. Davis, Z. W., Muller, L., Martinez-Trujillo, J., Sejnowski, T. & Reynolds, J. H. Spontaneous travelling cortical waves gate perception in behaving primates. *Nature* **587**, (2020).

70. Babiloni, F. *et al.* Spline Laplacian estimate of EEG potentials over a realistic magnetic resonance-constructed scalp surface model. *Electroencephalogr Clin Neurophysiol* **98**, (1996).

71. Bahramisharif, A. *et al.* Propagating neocortical gamma bursts are coordinated by traveling alpha waves. *Journal of Neuroscience* **33**, (2013).

72. Halgren, M. *et al.* The generation and propagation of the human alpha rhythm. *Proc Natl Acad Sci U S A* **116**, (2019).

73. Lozano-Soldevilla, D. & VanRullen, R. The Hidden Spatial Dimension of Alpha: 10-Hz Perceptual Echoes Propagate as Periodic Traveling Waves in the Human Brain. *Cell Rep* **26**, (2019).

74. Ermentrout, G. B. & Kleinfeld, D. Traveling electrical waves in cortex: insights from phase dynamics and speculation on a computational role. *Neuron* **29**, 33–44 (2001).

75. Feller, M. B., Wellis, D. P., Stellwagen, D., Werblin, F. S. & Shatz, C. J. Requirement for cholinergic synaptic transmission in the propagation of spontaneous retinal waves. *Science (1979)* **272**, 1182–1187 (1996).

76. Ackman, J. B., Burbridge, T. J. & Crair, M. C. Retinal waves coordinate patterned activity throughout the developing visual system. *Nature* **490**, (2012).

77. Zheng, J., Lee, S. & Zhou, Z. J. A transient network of intrinsically bursting starburst cells underlies the generation of retinal waves. *Nat Neurosci* **9**, 363–71 (2006).

78. Newman, E. a & Zahs, K. R. Calcium waves in retinal glial cells. *Science* **275**, 844–7 (1997).

79. Hanganu, I. L., Ben-Ari, Y. & Khazipov, R. Retinal waves trigger spindle bursts in the neonatal rat visual cortex. *Journal of Neuroscience* **26**, (2006).

80. Chen, Z. J., He, Y., Rosa-Neto, P., Germann, J. & Evans, A. C. Revealing modular architecture of human brain structural networks by using cortical thickness from MRI. *Cereb Cortex* **18**, 2374–81 (2008).

81. Liang, Y. *et al.* Complexity of cortical wave patterns of the wake mouse cortex. *Nat Commun* **14**, 1434 (2023).

82. Liang, Y. *et al.* Cortex-wide dynamics of intrinsic electrical activities: Propagating waves and their interactions. *Journal of Neuroscience* **41**, (2021).

83. van den Berg, D., Gong, P., Breakspear, M. & van Leeuwen, C. Fragmentation: Loss of global coherence or breakdown of modularity in functional brain architecture? *Front Syst Neurosci* **6**, 20 (2012).

84. Sloviter, R. S. Decreased hippocampal inhibition and a selective loss of interneurons in experimental epilepsy. *Science (1979)* **235**, (1987).

85. Nietz, A. K. *et al.* To be and not to be: wide-field Ca2+ imaging reveals neocortical functional segmentation combines stability and flexibility. *Cerebral Cortex* **33**, 6543–6558 (2023).

86. Afrashteh, N., Inayat, S., Mohsenvand, M. & Mohajerani, M. H. Optical-flow analysis toolbox for characterization of spatiotemporal dynamics in mesoscale optical imaging of brain activity. *Neuroimage* **153**, (2017).

87. Ali, F. & Kwan, A. C. Interpreting in vivo calcium signals from neuronal cell bodies, axons, and dendrites: a review. *Neurophotonics* **7**, (2019).

88. Zhang, Y. *et al.* Rapid detection of neurons in widefield calcium imaging datasets after training with synthetic data. *Nat Methods* **20**, 747–754 (2023).

89. Shemesh, O. A. *et al.* Precision Calcium Imaging of Dense Neural Populations via a Cell-Body-Targeted Calcium Indicator. *Neuron* **107**, (2020).

90. Chemla, S. *et al.* Improving voltage-sensitive dye imaging: with a little help from computational approaches. *Neurophotonics* **4**, (2017).

91. Nunez, P. L. & Srinivasan, R. A theoretical basis for standing and traveling brain waves measured with human EEG with implications for an integrated consciousness. *Clinical Neurophysiology* **117**, (2006).

92. Pang, J. C. *et al.* Geometric constraints on human brain function. *Nature* **618**, 566–574 (2023).